Topology Optimization of Smart Structures to Enhance the Performances of Vibration Control and Energy Harvesting

J. P. Sena [1,2], A. M. G. de Lima [1], N. Bouhaddi [2], N. Kacem [2]

[1] Federal University of Uberlândia, Faculty of Mechanical Engineering, Uberlândia, Brazil

[2] University of Franche-Comté, CNRS, FEMTO-ST Institute, Department of Applied Mechanics, Besançon

E-mail: `joaopedrosena@ufu.br`

Mars 2024

Abstract. With the growing interest in smart materials, the utilization of shunted piezoceramics for dynamic vibration control has gained significant attention due to their unique characteristics, such as the ability to absorb strain energy from vibrating systems and convert it into electrical energy. Designing and analyzing the behavior of structures in hybrid mitigation/harvesting conditions, considering both reliability and performance, pose challenges. This paper aims to achieve optimal design parameters for the structure by employing a multiobjective optimization approach that strikes a compromise between maximizing harvested power and minimizing structural damage. To evaluate the effectiveness of the design, topology optimization was conducted in three different cases to compare the results. By systematically exploring the design space, these cases provide insights into the influence of various parameters on the structural performance. Furthermore, to enhance computational efficiency, the structure was represented as a metamodel using neural networks. This approach enables rapid evaluation and prediction of the structure's behavior, facilitating the optimization process. By integrating multiobjective optimization, topology optimization, and metamodeling techniques, this study aims to provide valuable insights into the optimal design of structures that simultaneously incorporate shunt circuitry for vibration control and energy harvesting, leading to improved performance and reliability.

Keywords: Harvesting, Fatigue, Topology optimization, Shunt Circuit

1. Introduction

High cycle vibrations engender fatigue damage in mechanical structures, thereby altering the structural stiffness and accelerating wear and product failure [1]. Numerous control techniques have been suggested across various engineering disciplines to alleviate these vibrations [2]. Among the various approaches, the use of smart materials has recently garnered significant research attention. Shunted piezoceramics, in particular, have demonstrated wide-ranging applications due to their distinctive characteristics [3], such as the ability to absorb strain energy from a vibrating system and convert it into electrical energy, which can be harnessed to power electronic devices [4; 5]. Consequently, vibrating energy harvesting (VEH) has emerged as a promising alternative for small-scale devices, particularly for aeronautical vehicles that necessitate a limited amount of operational energy [6].

Both vibration control and vibration energy harvesting problems require a tuning of their respective circuits in order to obtain an effective output. For shunt circuits, although there's direct methods which don't require optimization routines to achieve good parameters [7], the majority of studies on the parameter tuning propose some sort of optimization methodology [8–10]. The same issue is faced when considering the parameters of an vibration energy harvester, since the circuit configuration is essential to reduce internal energy dissipation, obtain impedance matching and improve energy conversion efficiency [11; 12]. Recent research highlights the deliberate integration of nonlinearities in vibration energy harvesters, offering potential performance improvements in ambient conditions compared to linear resonant counterparts [13–15].

An interesting methodology used to improve the structural performance at the initial phase of the conceptual design is the topology optimization. In recent years, it has garnered significant attention due to its potential applications in the development of advanced electromechanical systems. Various solution approaches, such as the PEMAP-P (piezoelectric material with penalization and polarization) [16; 17], SIMP (solid isotropic material with penalization) [18] and MMA (method of moving asymptotes) [19] have been explored. The use of gradient-based mathematical programming [20] and genetic algorithms (GA) [21], including other methods such as Sequential Linear Programming (SLP) [22], were also used to solve the topology optimization problems for PZT (piezoelectric) structures.

The consideration of piezoelectric material properties in the structure has been investigated using techniques such as parametric placement [23–25] and density of the piezoelectric layer, for vibration control [26] and energy harvesting [27]. These comprehensive investigations contribute to the advancement of topology optimization techniques for piezoelectric structures. Hence, the aim of this work is to propose an optimal topological design of a vibration energy harvester device reducing the fatigue reliability and vibration of the smart structure with the shunt/conversion circuit.

2. Structural modelling

Considering a beam and a plate with fixed-free conditions for analysis, with a structure layer and a piezoelectric layer, we have two cases to be analyzed regarding the electromechanical coupling. The shunt/harvester circuit is connected to the piezoelectric layer for each case. A resistive circuit are considered in this analysis, with a schematic shown in figure 1.

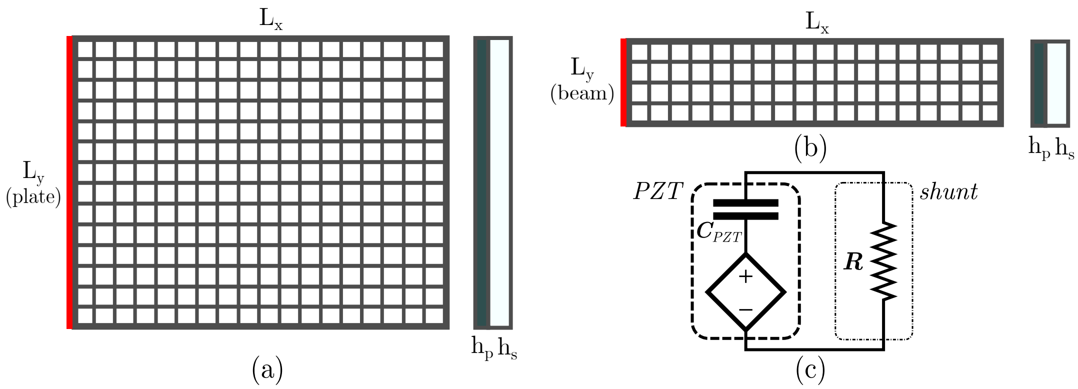

Figure 1: Components of the structure (a) Plate (b) Beam (c) Resistive circuit.

2.1. Electromechanical formulation

In accordance with Hamilton's variational principle, the finite element method yields formulations for the kinetic energy and the strain potential energy of an electromechanical system, as seen in 1. The mechanical degrees of freedom $\boldsymbol{U}$, density ρ and volume V_{e} of the element compose the kinetic energy, while the strain potential energy is constituted of of the strain $\boldsymbol{\varepsilon}$ and the stress $\boldsymbol{\sigma}$, the electric field $\boldsymbol{E}$ and the electrical displacements $\boldsymbol{D}$.

$$E_{\mathrm{c}} = \frac{1}{2}\int_{V_{\mathrm{e}}} \rho \dot{\boldsymbol{U}}^{\mathsf{T}} \dot{\boldsymbol{U}} \, \mathrm{d}V_{\mathrm{e}} \quad , \qquad E_{\varepsilon} = \int_{V_{\mathrm{e}}} \left(\boldsymbol{\varepsilon}^{\mathsf{T}} \boldsymbol{\sigma} - \boldsymbol{E}^{\mathsf{T}} \boldsymbol{D} \right) \mathrm{d}V_{\mathrm{e}}. \tag{1}$$

A linear equation system of the electromechanical coupling involves utilizing material characteristics, such as the mechanical properties $\boldsymbol{C}$, dielectric constants $\boldsymbol{e}$, and electric permittivity $\boldsymbol{\chi}$, to establish relationships between stress and electrical displacement, as well as strain and electric field, respectively:

$$\left\{ \begin{array}{c} \boldsymbol{\sigma} \\ \boldsymbol{D} \end{array} \right\} = \left[\begin{array}{cc} \boldsymbol{C} & -\boldsymbol{e}^{\mathsf{T}} \\ \boldsymbol{e} & \boldsymbol{\chi} \end{array} \right] \left\{ \begin{array}{c} \boldsymbol{\varepsilon} \\ \boldsymbol{E} \end{array} \right\}. \tag{2}$$

The interpolation functions $\boldsymbol{N}$ and the matrix $\boldsymbol{A}_{\mathrm{u}}$, which establishes the relationship between degrees of freedom and displacement field, are employed in conjunction with the kinetic energy to define the elementary mass matrix. In a similar manner, the elementary stiffness matrices are computed by incorporating the potential energy and the electromechanical coupling alongside the matrix $\boldsymbol{B}_{\{\bullet\}}$, which establishes the connection between the interpolation functions and the strain field based on the principles of linear elasticity theory. Considering the discrete equivalent layers theory, the cumulative mass and stiffness contributions from each layer are aggregated to portray the behaviour of the element, extending until the n-th layer:

$$
\begin{aligned}
\boldsymbol{M}^{\{e\}} &= \sum_{k=1}^{n} \int_{V_k} \rho_k \boldsymbol{N}^{\mathsf{T}} \boldsymbol{A}_{\mathrm{u}}^{\mathsf{T}} \boldsymbol{A}_{\mathrm{u}} \boldsymbol{N} \, \mathrm{d}V_k & \boldsymbol{K}_{\mathrm{u}\phi}^{\{e\}} &= \sum_{k=1}^{n} \int_{V_k} \boldsymbol{B}_{\mathrm{u}}^{\mathsf{T}} \boldsymbol{e} \boldsymbol{B}_{\phi} \, \mathrm{d}V_k \\
\boldsymbol{K}_{\mathrm{uu}}^{\{e\}} &= \sum_{k=1}^{n} \int_{V_k} \boldsymbol{B}_{\mathrm{u}}^{\mathsf{T}} \boldsymbol{C} \boldsymbol{B}_{\mathrm{u}} \, \mathrm{d}V_k & \boldsymbol{K}_{\phi\phi}^{\{e\}} &= \sum_{k=1}^{n} \int_{V_k} -\boldsymbol{B}_{\phi}^{\mathsf{T}} \chi \boldsymbol{B}_{\phi} \, \mathrm{d}V_k
\end{aligned}
\tag{3}
$$

It is important to notice that the relation $\boldsymbol{K}_{\phi\mathrm{u}} = \boldsymbol{K}_{\mathrm{u}\phi}^{\mathsf{T}}$ occurs by the characteristic symmetry. The global electromechanical dynamic system shown in 4 relates the displacement $\boldsymbol{u}(t)$ and potential energy $\boldsymbol{\phi}(t)$ with an external force $\boldsymbol{f}(t)$ and electrical charge $\boldsymbol{q}(t)$ in the time domain [28]. A proportional Rayleigh's damping $\boldsymbol{C}_{\mathrm{eq}} = \alpha \boldsymbol{M} + \beta \boldsymbol{K}_{\mathrm{uu}}$ is considered.

$$
\begin{bmatrix} \boldsymbol{M} & 0 \\ 0 & 0 \end{bmatrix} \begin{Bmatrix} \ddot{\boldsymbol{u}} \\ \ddot{\boldsymbol{\phi}} \end{Bmatrix} + \begin{bmatrix} \boldsymbol{C}_{\mathrm{eq}} & 0 \\ 0 & 0 \end{bmatrix} \begin{Bmatrix} \dot{\boldsymbol{u}} \\ \dot{\boldsymbol{\phi}} \end{Bmatrix} + \begin{bmatrix} \boldsymbol{K}_{\mathrm{uu}} & \boldsymbol{K}_{\mathrm{u}\phi} \\ \boldsymbol{K}_{\phi\mathrm{u}} & \boldsymbol{K}_{\phi\phi} \end{bmatrix} \begin{Bmatrix} \boldsymbol{u} \\ \boldsymbol{\phi} \end{Bmatrix} = \begin{Bmatrix} \boldsymbol{f} \\ \boldsymbol{q} \end{Bmatrix}. \tag{4}
$$

Assuming an harmonic motion in the system, with $\boldsymbol{u}(t) = \boldsymbol{U}_0 \exp(\mathrm{i}\omega t)$, $\boldsymbol{\phi}(t) = \boldsymbol{\Phi}_0 \exp(\mathrm{i}\omega t)$, $\boldsymbol{f}(t) = \boldsymbol{F}_0 \exp(\mathrm{i}\omega t)$ and $\boldsymbol{q}(t) = \boldsymbol{Q}_0 \exp(\mathrm{i}\omega t)$, the complex Frequency Response Function (FRF) of the displacement and voltage (potential) are given by the following equations, respectively:

$$
\boldsymbol{H}_{\mathrm{u}}(\omega) = \left[\boldsymbol{KCM} - \boldsymbol{K}_{\mathrm{u}\phi} \left(\boldsymbol{K}_{\phi\phi} - \frac{1}{\mathrm{i}\omega \boldsymbol{Z}} \right)^{-1} \boldsymbol{K}_{\phi\mathrm{u}} \right]^{-1}, \tag{5}
$$

$$
\boldsymbol{H}_{\phi}(\omega) = \left[\boldsymbol{K}_{\phi\mathrm{u}} \boldsymbol{KCM}^{-1} \boldsymbol{K}_{\mathrm{u}\phi} + \frac{1}{\mathrm{i}\omega \boldsymbol{Z}} - \boldsymbol{K}_{\phi\phi} \right]^{-1} \boldsymbol{K}_{\phi\mathrm{u}} \boldsymbol{KCM}^{-1}. \tag{6}
$$

The item $\boldsymbol{KCM} = (\boldsymbol{K}_{\mathrm{uu}} + \mathrm{i}\omega \boldsymbol{C}_{\mathrm{eq}} - \omega^2 \boldsymbol{M})$ is used for easier representation. The output power of the system is considered by calculating the power of the shunt/conversion circuit ($P = V^2/R$), and the average output power in 7 is calculated considering one vibration cycle of the frequency ω, with $\overline{H}_{\phi}$ as the scalar voltage of the connection point in the piezoceramic layer. The average output power is used as the harvested energy parameter in the multiobjective optimization process.

$$
P_{\mathrm{av}} = \frac{1}{2} \frac{\overline{H}_{\phi}^{2}}{R}. \tag{7}
$$

2.2. Fatigue reliability

Derived from the findings of [29], this multiaxial criteria aims to design engineering structures based on the endurance limit at 10^6 cycles or more. The Sines' criterion provides good predictions, and is based on the equivalent shear stress amplitude (square root of the second invariant amplitude) $\sqrt{J_{2,\mathrm{a}}}$, endurance limit for the torsion stress $\tau_{\_1}$, material constant ratio m and mean hydrostatic stress $\mathbb{E}\left[p_{\mathrm{h}}(t)\right]$ [30]:

$$
\sqrt{J_{2,\mathrm{a}}} \leq f_{\mathrm{eq}} = \tau_{\_1} - (3m - \sqrt{3}) \mathbb{E}\left[p_{\mathrm{h}}(t)\right]. \tag{8}
$$

Considering the second invariant of the deviatoric stress tensor in a five-dimensional Euclidean space E_5, and fixing each dimension as the semi-axes of the five dimension prismatic hull circumscribed to the loading path of the second invariant, the equivalent shear stress amplitude is calculated by the euclidean distance of each semi-axes coordinate [29]. Considering a random state $\mathfrak{X}$ for the random equivalent shear stress amplitude, the deterministic second invariant is now represented as $\sqrt{\mathfrak{J}_{2,\mathrm{a}}}$:

$$\sqrt{J_{2,\mathrm{a}}} = \sqrt{R_1^2 + R_2^2 + R_3^2 + R_4^2 + R_5^2} \Rightarrow \mathfrak{X} \Rightarrow \sqrt{\mathfrak{J}_{2,\mathrm{a}}} = \sqrt{\mathfrak{R}_1^2 + \mathfrak{R}_2^2 + \mathfrak{R}_3^2 + \mathfrak{R}_4^2 + \mathfrak{R}_5^2}. \quad (9)$$

The Gumbel distributions are used as base to calculate $\sqrt{\mathfrak{J}_{2,\mathrm{a}}}$ [29]. Considering that the variables $\mathfrak{R}_i$ are not correlated, the expectancy and variance of $\left(\sqrt{\mathfrak{J}_{2,\mathrm{a}}}\right)^2$ are equal to $\sum \mathbb{E}\left[\mathfrak{R}_i^2\right]$ and $\sum \mathbb{V}\left[\mathfrak{R}_i^2\right]$ respectively.

Using the statistical moments definitions, Apery's constant $\zeta_3 \approx 1.202\,06$ and the definition of variance $\mathbb{V}\left[\sqrt{\mathfrak{J}_{2,\mathrm{a}}}\right] = \mathbb{E}\left[\left(\sqrt{\mathfrak{J}_{2,\mathrm{a}}}\right)^2\right] - \mathbb{E}\left[\sqrt{\mathfrak{J}_{2,\mathrm{a}}}\right]^2$:

$$\begin{aligned}\mathbb{E}\left[\mathfrak{J}_{2,\mathrm{a}}\right]^2 - 4\mathbb{E}\left[\sqrt{\mathfrak{J}_{2,\mathrm{a}}}\right]^2 \left(\mathbb{E}\left[\mathfrak{J}_{2,\mathrm{a}}\right] - \mathbb{E}\left[\sqrt{\mathfrak{J}_{2,\mathrm{a}}}\right]^2\right) - \frac{22}{5}\left(\mathbb{E}\left[\mathfrak{J}_{2,\mathrm{a}}\right] - \mathbb{E}\left[\sqrt{\mathfrak{J}_{2,\mathrm{a}}}\right]^2\right)^2 - \\ -48\zeta_3 \frac{\sqrt{6}}{\pi^3}\mathbb{E}\left[\sqrt{\mathfrak{J}_{2,\mathrm{a}}}\right]\left(\mathbb{E}\left[\mathfrak{J}_{2,\mathrm{a}}\right] - \mathbb{E}\left[\sqrt{\mathfrak{J}_{2,\mathrm{a}}}\right]^2\right)^{3/2} + \mathbb{V}\left[\mathfrak{J}_{2,\mathrm{a}}\right] = 0. \quad (10)\end{aligned}$$

Finally, a Newton-Raphson methodology is used to solve for $\mathbb{E}\left[\sqrt{\mathfrak{J}_{2,\mathrm{a}}}\right]$, assuming an initial estimation of $\mathbb{E}\left[\sqrt{\mathfrak{J}_{2,\mathrm{a}}}\right] \approx \sqrt{\mathbb{E}\left[\mathfrak{J}_{2,\mathrm{a}}\right]}$. The result of this solution is used as a mean damage indicator in the multiobjective optimization to minimize the structural damage.

2.3. Circuit optimization

The harvester performance directly depends on the values of the circuit parameters of figure 1c. These values are not necessarily the same for the shunt circuit, implying the necessity of an optimization routine to tune the circuit for the best compromise between the two objectives. Considering an structure with an unimorph configuration (i.e., one complete piezoceramic layer), and employing this scenario as the reference circuit case, an optimization procedure is conducted, wherein the circuit parameters serve as the project variables:

$$\begin{aligned}&\min_{R} \quad \left\{f_1 = -P_{\mathrm{av}} \quad , \quad f_2 = \mathbb{E}\left[\sqrt{\mathfrak{J}_{2,\mathrm{a}}}\right]\right\}, \\ &\text{s.t.} \quad R_{\min} < R \leq R_{\max} \qquad \in \mathbb{R}\ .\end{aligned} \quad (11)$$

Using an Non-dominated Sorting Genetic Algorithm (NSGA-II) for the optimization process with a population of 100 and 200 generations, the solution population results in a pareto's curve of figure 3. The best compromise between the objectives in the beam case is when $R = 6.6$ kΩ, and $R = 1.8$ kΩ for the plate. In both cases, higher values of resistance resulted in higher values of resulting harvesting power.

3. Topology optimization

The topology optimization process is divided in three cases. In each one, the topology change in the function evaluation step, and therefore requires a new model reduction process to be applied in the mechanical and electrical matrices. Due to the matrix dimensions of the problem, the processing time necessary to evaluate the optimization function becomes substantial, requiring the use of an alternative numerical method.

3.1. Metamodeling

Using a Feedfoward Neural Network as an alternative for metamodeling the dynamic behaviour of the structure, it is possible to represent the power output and the fatigue parameter as a tensor operation, where the weights of this network are trained by the backpropagation method using a previously calculate dataset [31]. An Encoder-Decoder architecture is proposed to extract topology features throughout the hidden layers [32].

Here, the standardized input values are the variables of the circuit and the density of the piezoelectric layer of each element of the finite element model, and the output values are the energy and fatigue optimization parameters, as seen in figure 2. A total of $1.1 \cdot 10^4$ and $5.0 \cdot 10^4$ solutions are used to train the network for the beam and plate structural type respectively, and a dropout layer is used to avoid overfitting. The loss function chosen for the backpropagation algorithm is the Mean Squared Error (MSE).

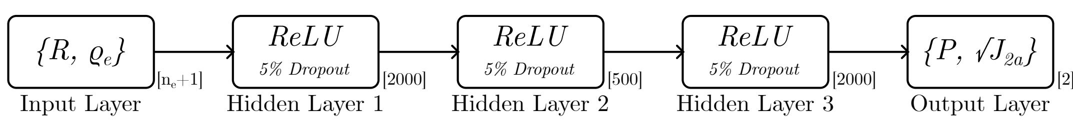

Figure 2: Neural Network architecture with n_{e} as the number of elements of the structure

After 50 epochs (with an early stopping criteria), the model is capable of representing the structure behaviour with a mean of 0.015 and 0.04 MSE for the beam and plate model. Using the metamodel in a 10 generations optimization of a plate example took 2.4 minutes to find the results, in contrast to 8.3 hours with the conventional objective function calculation. The experiment was conducted in a personal computer with a 4 core Intel i5 processor running at 1.60 GHz using 8 GB of RAM.

3.2. Strain energy

As observed in previous studies on energy harvesting, the incorporation of patches is determined by the fabrication procedure of the piezoelectric ceramic. Consequently, a clever approach for patch integration involves strategically positioning it in regions exhibiting elevated levels of modal strain energy $\boldsymbol{\Xi} = \boldsymbol{\Phi}_i^{\mathsf{T}} \boldsymbol{K} \boldsymbol{\Phi}_i$, where $\boldsymbol{\Phi}_i$ is the modal displacement of the i-th mode [33]. Considering the structures of figure 1, the modal strain energy is calculated for each type. The criteria for piezoelectric placement follows the percentage of strain energy, where the placement is done in the region that covers

60% percent of the total modal strain energy, resulting in the configuration of a single patch covering the elements close to the support region for both structures.

3.3. Patch distribution

A second approach is done, now considering the placement of piezoelectric patches in the structure. The number of rectangular patches are parametrically defined before optimization. The new constraints added to the optimization problem describe the distance between the patches (dx and dy) and the length of the patches on each direction (px and py). These variables correspond to the number of elements in the finite element model, therefore $p, d \in \mathbb{Z}$. The subscript in d_{ij} and p_{ij} corresponds to the location on the i-th line in the principal direction and the j-th line in the secondary direction. In the general case, the additional constraints are:

$$\begin{cases} 0 \leq dx_{ij} \leq dx_{\max} \quad , \quad 1 \leq px_{ij} \leq px_{\max} \qquad \forall_{i\in\{1,\ldots,n_{\mathrm{x}}\}\wedge j\in\{1,\ldots,n_{\mathrm{y}}\}} \\ 0 \leq dy_{ij} \leq dy_{\max} \quad , \quad 1 \leq py_{ij} \leq py_{\max} \qquad \forall_{i\in\{1,\ldots,n_{\mathrm{y}}\}\wedge j\in\{1,\ldots,n_{\mathrm{x}}\}} \end{cases}, \tag{12}$$

with n_{y} as the number o patches in the x and y directions, respectively. The number max of each parameter is carefully calculated based on the number of patches chosen and a maximum cover percentage of the piezoelectric layer. In the beam case, a one dimension version is applied and the constraints in the y direction are not considered.

3.4. Density of PZT layer

This methodology is used to define a nonlinear distribution of the piezoelectric layer through the structure. To do so, the influence of the piezoelectric material of each element is accounted by the binary presence or not of the layer ($\rho \in \mathbb{Z}_2$) and its contribution to the mechanical and electrical global matrices for the total number of elements e in the structure:

$$\begin{aligned} \boldsymbol{M}^{\{e\}} &= \boldsymbol{M}^{\{e\}}_{\mathrm{st}} + \rho_e \boldsymbol{M}^{\{e\}}_{\mathrm{pzt}}, \qquad & \boldsymbol{K}^{\{e\}}_{\mathrm{u}\phi} &= \rho_e \boldsymbol{K}^{\{e\}}_{\mathrm{u}\phi,\mathrm{pzt}}, \\ \boldsymbol{K}^{\{e\}}_{\mathrm{uu}} &= \boldsymbol{K}^{\{e\}}_{\mathrm{uu,st}} + \rho_e \boldsymbol{K}^{\{e\}}_{\mathrm{uu,pzt}}, \qquad & \boldsymbol{K}^{\{e\}}_{\phi\phi} &= \rho_e \boldsymbol{K}^{\{e\}}_{\phi\phi,\mathrm{pzt}}. \end{aligned} \tag{13}$$

In addition to the problem in 11, the constraints $\sum \rho_e V_e - f_{\mathrm{V}} \sum V_e \leq 0$ is added for each element e, with f_{V} equals to the maximum cover percentage and $\rho \in \{0, 1\}$.

4. Results and discussion

Using the same population and generations as the circuit optimization for the three studied cases, the pareto's fronts in figure 3 are found for the beam and plate. The non-continuity in the curves of patches and density cases can be attributed to the nonlinearity added with the topology change throughout the optimization process. The abrupt changes in the patches' curve can be linked to mesh discretization, when a small change in the configuration of elements results in a great shift in the objective functions.

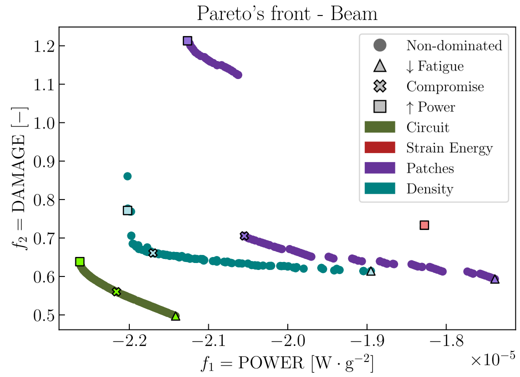

(a)

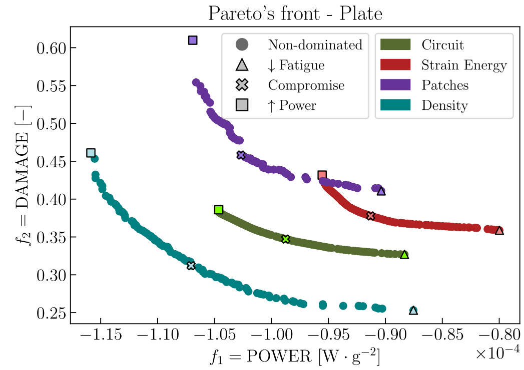

(b)

Figure 3: Results for the three cases and the circuit in (a) Beam and (b) Plate

In both structures, the patch distribution alongside the strain energy have the worst non-dominated results. In the beam, the strain energy consists in only one point, indicating the maximum resistance for all non-dominated solutions. Also, solutions with higher harvested power have a fatigue indicator greater than one, which implies a failure of this structure. For the plate, although other fronts dominate the patches, one can notice that it can harvest more energy in the extreme upper solutions than the circuit reference case. As for the density case, results only outperform the others in the plate structure. It is important to highlight its better performance relative to the reference circuit optimization, even with less piezoelectric material and therefore less weight added to the structure. Finally, the resulting distribution of piezoelectric layer is presented in the figure 4, for the patches and density of layer cases of each structure.

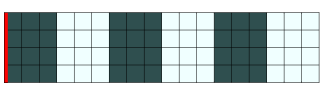

(a) $R = 7.99$ kΩ

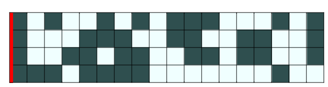

(b) $R = 9.99$ kΩ

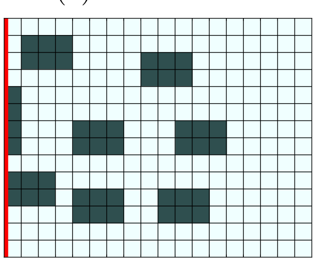

(c) $R = 3.22$ kΩ

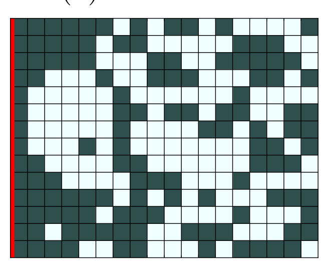

(d) $R = 2.44$ kΩ

Figure 4: Distribution of Beam (a) patches, (b) density; Plate (c) patches, (d) density.

The compromise of solutions for the patches case show a more sparse concentration for the beam and a more centralized location for the plate. Throughout the solutions curve, we observed a translation from the placement closer to the fixed support to a middle-right area. This solutions shown result in a middle ground configuration for minimizing the fatigue and maximizing the harvested power.

As for the density layer case, although the presence of some randomized forms of the PZT layer, it is clear the sparse concentration in small regions in all of the beam's length, following the same logic of the patches case. For the plate, the solution has a big region closer to the fixed support that assimilates the region with higher modal energy. In the rest of the structure, some gaps appear in the middle area together with small regions in the free edge.

5. Conclusion

The use of metamodeling through neural networks in the genetic algorithm has shown a great improvement in the optimal design of smart structures, enabling different types of analyzes to be carried out with a single model. A robust model is necessary to insert real values of the circuit together with binary values of the topology, although it makes it possible to perform more complex problems.

The pareto's fronts shows that the parametric analysis of the patch placement only outperform the strain energy case, showing a result improvement when rearranging the PZT layer on the surface of the structures. Despite the gain in performance, the conception complexity of the problem can greatly increase with higher number of patches, which has to be taken into account in the designing phase.

The results also show better performance of the density layer case in comparison with the other optimizations. Even the reference circuit optimization in the plate is outperformed, revealing enhancement in the fatigue and energy harvested regardless of the discontinuous layer shape. When the amount of PZT material is critical, such as applications which structural mass greatly influences the mechanical application, the density optimization design strategy presents itself as a promising alternative.

In future works, the use of different structural configurations and boundary conditions may show other layer patterns. A different multimodal shunt circuit may also help increase the resulting curve, as well as the use of a layer filter such as a kernel or convolution in the optimization problem, enabling the application in experiments.

6. Acknowledgements

This study was financed in part by the Coordenação de Aperfeiçoamento de Pessoal de Nível Superior - Brasil (CAPES) – Finance Code 88887.696945/2022-00, and has been performed in cooperation with the EUR EIPHI program (ANR 17-EURE-0002).

References

[1] Montalvao D 2006 *The Shock and Vib. Dig.* **38** 295–324

[2] Balaji P S and SelvaKumar K K 2020 *J. of Vib. Eng. Technol.* **9** 183–213

[3] Gripp J and Rade D 2018 *Mech. Syst. and Signal Process.* **112** 359–383

[4] Marqui C D, Vieira W G R, Erturk A and Inman D J 2010 *J. of Vib. and Acoust.* **133**

[5] Erturk A 2011 *Piezoelectric energy harvesting* (Wiley) ISBN 9780470682548

[6] Li D, Wu Y, Ronch A D and Xiang J 2016 *Prog. in Aerosp. Sci.* **86** 28–62

[7] Raze G, Paknejad A, Zhao G, Collette C and Kerschen G 2020 *J. of Intell. Mater. Syst. and Struct.* **31** 1731–1747

[8] Viana F A C and Valder Steffen J 2006 *J. of the Braz. Soc. of Mech. Sci. and Eng.* **28** 293–310

[9] Marakakis K, Tairidis G K, Foutsitzi G A, Antoniadis N A and Stavroulakis G E 2022 *Signals* **3** 830–856

[10] Aouali K, Kacem N, Bouhaddi N and Haddar M 2021 *Actuators* **10** 25

[11] Zhang B, Liu H, Hu B and Zhou S 2022 *Smart Mater. and Struct.* **31** 095040

[12] Schoeftner J and Buchberger G 2013 *Eng. Struct.* **53** 92–101

[13] Mahmoudi S, Kacem N and Bouhaddi N 2014 *Smart Mater. and Struct.* **23** 075024

[14] Drezet C, Kacem N and Bouhaddi N 2018 *Sens. and Actuators A: Phys.* **283** 54–64

[15] Aouali K, Kacem N and Bouhaddi N 2022 *Sens.* **22** 7657

[16] Kögl M and Silva E C N 2005 *Smart Mater. and Struct.* **14** 387–399

[17] Nakasone P and Silva E 2010 *J. of Intell. Mater. Syst. and Struct.* **21** 1627–1652

[18] Guzmán D G, Silva E C N and Rubio W M 2020 *Smart Mater. and Struct.* **29**

[19] Homayouni-Amlashi A, Schlinquer T, Mohand-Ousaid A and Rakotondrabe M 2020 *Struct. and Multidiscip. Optim.* **63** 983–1014

[20] Kang Z and Wang X 2010 *Smart Mater. and Struct.* **19** 075018

[21] Wang S Y, Tai K and Quek S T 2006 *Smart Mater. and Struct.* **15** 253–269

[22] Silva E C N and Kikuchi N 1999 *Smart Mater. and Struct.* **8** 350–364

[23] da Silva L P, Larbi W and Deü J F 2014 *J. of Intell. Mater. Syst. and Struct.* **26** 1219–1235

[24] Mello L A M, Kiyono C Y, Nakasone P H and Silva E C N 2014 *Smart Mater. and Struct.* **23** 025035

[25] Zhang X, Kang Z and Li M 2014 *Struct. and Multidiscip. Optim.* **50** 799–814

[26] Zhang X and Kang Z 2013 *J. of Intell. Mater. Syst. and Struct.* **25** 697–712

[27] Zheng B, Chang C J and Gea H C 2009 *Struct. Multidiscip. Optim.* **38** 17–23

[28] de Lima A, Lambert S, Rade D, Pagnacco E and Khalij L 2014 *Mech. Syst. and Signal Process.* **43** 305–318

[29] Lambert S, Pagnacco E and Khalij L 2010 *Int. J. of Fatigue* **32** 463–474

[30] Papadopoulos I 1997 *Int. J. of Fatigue* **19** 219–235

[31] von Wysocki T, Rieger F, Tsokaktsidis D E and Gauterin F 2021 *Des.* **5** 36

[32] Sajedi S O and Liang X 2019 *Comput.-Aided Civ. and Infrastruct. Eng.* **35** 579–596

[33] Zhao J, Shi M, Yin G and Lian X 2020 *E3S Web of Conf.* **165** 06053